Laser treatment of 430 ferritic stainless steel for enhanced mechanical properties

Zhige Wang, Justin Dirrenberger, Pierre Lapouge, Sébastien Dubent

Laser treatment of 430 ferritic stainless steel for enhanced mechanical properties

Zhige Wang, Justin Dirrenberger *, Pierre Lapouge, Sébastien Dubent

Laboratoire PIMM, Arts et Metiers Institute of Technology, CNRS, Cnam, HESAM Université, 151 Boulevard de l'Hôpital, 75013, Paris, France

Keywords:
Laser heat treatment
Ferritic stainless steel
Hardening
Oxidation

A B S T R A C T

Thin AISI 430 ferritic stainless steel sheets containing 18% Cr were hardened by continuous-wave laser beams under different conditions. A symmetric double laser treatment platform was developed to operate two lasers simultaneously in order to achieve a homogenous microstructure through the specimen and avoid the overheating associated with single laser treatments on one surface. The influence of linear energy density and shielding gas on microstructure and hardness is investigated for both single and double laser treatments. Tensile behavior and oxidation effect during treatment are also studied. With a peak temperature around Tm, the single-track laser yields local microhardness that is 90% higher than the base material, while samples completely treated by the multi-track laser present a 60% increase in yield stress and 45.8% in ultimate tensile stress. These improvements in mechanical behaviors are driven by the formation of martensite and chromium carbides upon rapid cooling despite poor carbon content and dramatic grain coarsening. These results could be useful in order to locally modify the behavior of medium chrome ferritic stainless steel to meet industrial requirements.

1. Introduction

Ferritic stainless steels (FSS) are widely used in various domains, including automobile manufacturing, white goods, and nuclear power industries, as they exhibit a good combination of ductility, thermal conductivity, and corrosion resistance. Their cost is also relatively lower and more stable than austenitic grades, as they do not contain any nickel [1–3]. However, FSS also have several disadvantages. For example, they have a lower fracture strength and work hardening rate compared to austenitic stainless steels (ASS) [1], which restricts their industrial applications. Solutions include adding Mn to FSS to stabilize the austenitic microstructure at room temperature or assembling a hybrid form of ASS and FSS [2]. Furthermore, some surface thermal treatments such as nitriding or carburization can also reinforce the strength of the surface layer and thus improve their global mechanical performances [4].

Laser heat treatment is often used as a surface thermal treatment for numerous metallic materials on account of its rapid heating and cooling rates as well as its flexibility. Controlling the peak temperature or cooling rate can achieve different aims. For example, tempering or annealing can be achieved to increase the formability of steels. Capello et al. [5] reported an increase in ductility on dual-phase steel by laser tempering at temperatures below Ac1. Lapouge et al. [6] also studied tempering on steel with a high martensite content near Ac3 and found that the uniform plastic deformation was multiplied by a factor of 3 with optimal conditions. By contrast, the rapid cooling process can serve as quenching medium to strengthen the treated surface, increase the wear resistance, and extend the performance lifetime of the parts. Laser heat treatment on carbon steel bulks has been well studied to generate a thin protective layer of martensite on the surface [7].

Compared to martensitic stainless steels (MSS) and ASS, FSS are often considered to be poorly adapted to hardening by thermal treatment because of their poor carbon content [8]. Nevertheless, studies show that both traditional furnace and laser heat treatment can lead to a much higher microhardness and rupture strength. According to the different treatment conditions, this improvement in mechanical properties can be attributed to grain refining, intergranular and intragranular martensite formation, or carbide precipitations that appeared during the rapid cooling process [9–11]. However, laser heat treatment often yields significant grain coarsening in both the fusion zone and the heat affected zone (HAZ), with ductility and elongation being heavily reduced due to these changes [10].

Zhang et al. [2] studied the spot welding joint of AISI 430 steel and found that microhardness in the weld increased to around 300 Hv, although a special softened zone was found in the HAZ near the weld due to excessive grain coarsening. Dissimilar welding and filler welding

Nomenclature

Ac1	Critical temperature at which pearlite begins to transform into austenite during heating
Ac3	Critical temperature at which free ferrite is completely transformed into austenite during heating
c_p	Thermal conductivity
λ	Specific heat capacity
θ_a	Actual temperature
Tm	Melting temperature
Ms	Martensite start temperature
ΔG°	Gibbs free energy
$\sigma_{0.2\%}$	Yield stress
ε_u	Uniform plastic deformation

between FSS and ASS also show that when the temperature is around Ac3, the HAZ of FSS has a dual-phase ferrite and martensite microstructure and a much-improved hardness compared to the base material [12,13].

Vafaeian et al. [14] reported a study on FSS with cold-rolling and annealing near 800 °C (below Ac1) in a traditional furnace followed by water quenching. They obtained a nanoscale-refined microstructure and an ultimate tensile strength of around 1000 MPa but poorer ductility. Jha et al. [15] investigated the annealing of hot bands of FSS between Ac1 and Ac3 followed by water quenching and obtained around 18% volume fraction of martensite.

Sundqvist et al. [16] studied the continuous-wave fiber laser beam treatment on EN1.4003 FSS with both single and overlapping tracks. Their research focused on peak temperatures below 1500 °C and found that the hardness in the treated area could reach 350 Hv compared to 175 Hv in the base material. The characterization of weld joints was investigated on the same type of steel by Taban et al. [17]. No evident negative effect on mechanical behaviors was found in terms of tensile or bending resistance due to grain coarsening, although this reduced the local toughness of the welds.

Mahmoudi et al. [18] reported a surface treatment of an annealing AISI 420 MSS with a full ferritic microstructure and carbides by a pulsed ND:YAG laser. Their study achieved a 90% increase in surface hardness but also tempering in the overlapping zone, which caused a carbide deposit and less corrosion resistance in the grain boundaries. Pantsar et al. [19] studied diode laser hardening on low alloy steel and MSS and the effect of shielding gas during treatment. They found that the input energy required to attain Ac1 for treatment in air was significantly reduced with the presence of an oxidation layer, which could strongly depend on the base material and be difficult to control.

Even though numerous studies have reported on the mechanical properties of FSS welds and dissimilar welds between FSS and other stainless steels, few studies have explored the modification of the global mechanical properties of fully thermally treated FSS by laser heat treatment as well as the influence of operation conditions and parameters. In the present study, methodology was developed to use a continuous-wave laser as the thermal source to modify the mechanical properties of thin FSS sheets. A medium-chromium stainless steel AISI 430 was chosen for the study, as it presents a fully ferritic microstructure with chromium carbides inside the grains [20]. It is also one of the most widely used FSS in engineering.

2. Material and experimental procedures

Sheets of AISI 430 with a thickness of 0.5 mm and mirror-polished on both sides were used. To increase the absorption ratio of the laser beam, they were sand-blasted to obtain a uniform and matt finish. The chemical composition is shown in Table 1.

Table 1
Chemical composition [wt %] of the studied stainless steel AISI 430.

C	Si	Mn	Cr	Ni	P	Fe
0.026	0.30	0.50	18.70	0.14	0.03	Bal.

The laser treatment platform was set up as shown in Fig. 1. To achieve a more uniform treatment across the thickness of the sheets, two lasers were placed on each side to be used either simultaneously or separately. The two lasers available for this study are a single-mode 500 W fiber laser from SPI at a wavelength of 1080 nm (surface A) and a multimode 110 W laser diode from DILAS (surface B) operating at a wavelength of 980 nm. The sheets are fixed on a robotic arm that can freely move in space with a pre-programmed trajectory. The treatment can be operated under argon shielding gas to reduce oxide formation on the sheet surfaces at high temperatures. The spot size is defocused at 1 mm for surface A, and surface B is fixed at the focus distance where the spot size is 1.2 mm. Due to the different modalities of the two lasers, the energy density on surface A is much more intense than surface B at the beam center with the same input power. Thus, the impact on surface A penetrates deeper into the sheets than surface B, where the heated zone is more diffuse but shallow. Even though the spot size on surface B is larger than on surface A, microstructural results show that the treated zone is almost symmetric on both sides (Fig. 6).

The laser treatment parameters are shown in Table 2. For a given linear energy density (LED), the effects of a single laser and two symmetric double lasers are compared. For the highest linear energy density (25 kJ/m), an asymmetric parameter 150 W (surface A) + 100 W (surface B) is chosen for comparison with approximately 250 W on surface A because of the rather low-rated power of the diode laser (110 W). The linear velocity of the robotic arm is fixed at 10 mm/s for the entire study.

The temperature changes for the single laser treatment in Ar shielding gas were measured every millisecond with several type K thermocouples welded on the backside surface of the laser beam (surface B). The temperature on the beam side was not measured directly but instead simulated by the finite element method using the COMSOL Multiphysics software.

Microstructural observations were made on the cross-section before and after the laser treatment for both the single-track and multi-track using optical microscopy and scanning electron microscopy (SEM). Prior to the observations, the samples were prepared by grinding using silicon carbide abrasive papers with grit sizes of 240, 400, 800, and 1000, followed by cloth polishing using 9, 3, and 1 μm diamond suspension solutions, and finished with 0.04 μm colloidal silica suspension (OP–S). The samples were etched in Kalling's No.1 solution (1.5 g $CuCl_2$,

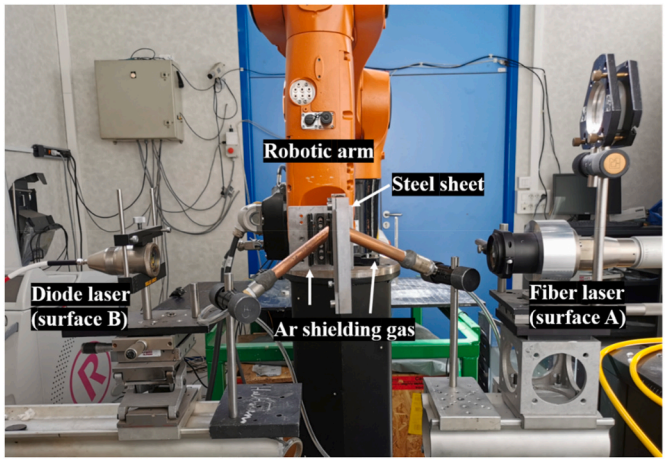

Fig. 1. Platform developed to heat treated thin sheets using a pre-programmed trajectory.

Table 2

Laser treatment parameters.

Laser	Single laser (surface A)		Double laser (surface A + surface B)		Linear velocity (mm/s)	Linear energy density (LED) P/V (kJ/m)
Shielding gas	Ar	Air	Ar	Air		
Power (W)	100	100	50 + 50	50 + 50	10	10
	150	150	75 + 75	75 + 75	10	15
	200	200	100 + 100	100 + 100	10	20
	250	250	150 + 100	150 + 100	10	25

33 ml HCl, 33 ml ethanol, 33 ml distilled water) for a few seconds to reveal the microstructure. The etching solution outlines the grain boundaries and turns the martensite into a dark brown color.

Vickers microhardness tests were performed along the middle line on the cross-section with a force of 100 gf and a load time of 10 s. Tensile tests were carried out on untreated and treated samples with dimensions as shown in Fig. 2. For treated samples, 10 laser tracks were applied at an interval of 1 mm, which theoretically corresponded to a fully covered gage section. Between each track, a cooling time of at least 30 s was set to minimize the heat-affected zone of the adjacent tracks.

To compare the effect of the argon shielding gas and air environment, the oxide layer on the surface of both sides was characterized by glow discharge optical emission spectrometry (GD-OES) using a Horiba JY 10000 RF spectrometer equipped with a 4-mm diameter anode. The argon pressure was 750 Pa, and the RF power was 40 W. The oxygen signal was especially monitored to identify the thickness of the oxide layer due to the laser treatment. Preliminary tests were carried out on both treated and untreated samples for 20 min in order to achieve a crater that was sufficiently deep to measure the eroded depth as accurately as possible by profilometry and thus determine the average sputtering rate of the surface.

3. Results

3.1. Thermal evolution measure and modeling

Fig. 3 describes the experimental and numerical temperature evolution at the beam center on the backside during the treatment at different LED. The temperature during the laser treatment is modeled with thermal conductivity (cp) and specific heat capacity (λ) calculated from the following equations [21], where θ_a is the actual temperature in °C, the melting temperature (Tm) is set at 1698 K, and the latent heat of fusion is 285 kJ/kg. Both laser beams were modeled as a Gaussian beam.

$$c_p = 450 + 0.280 \times \theta_a - 2.91 \times 10^{-4}\theta_a^2 + 1.34 \times 10^{-7}\theta_a^3 [\mathrm{J.kg^{-1}.K^{-1}}] \quad (1)$$

$$\lambda = 14.6 + 1.27 \times 10^{-2}\theta_a [\mathrm{W.m^{-1}.K^{-1}}] \quad (2)$$

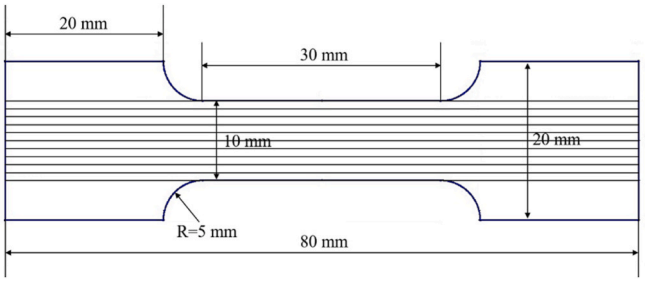

Fig. 2. Schematic sketch of the treated tensile test sample with dimensions.

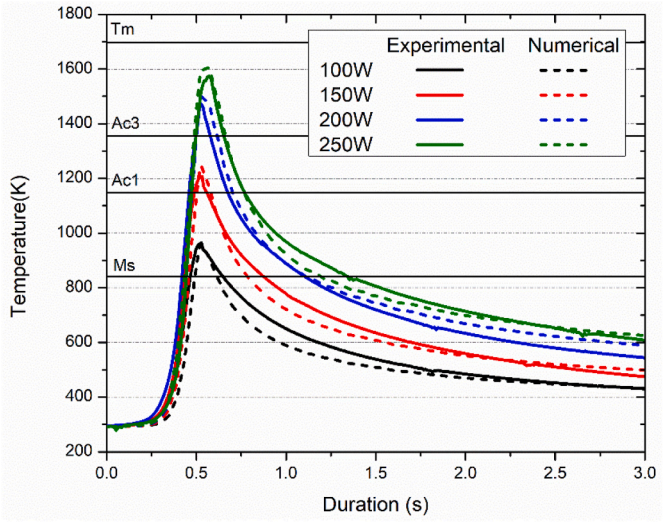

Fig. 3. Experimental measurements and simulation results of the backside temperature for the single laser treatment.

However, the coefficient of absorption depends on several factors such as the operating environment, the surface state, the wavelength of laser, the power, and so on. In this study, a value between 0.41 and 0.43 [19] is taken with Ar shielding gas after comparing the melting at the surface during treatment and Tm. While operating in air without shielding gas, the absorptivity is expected to increase by around 50% because of oxidation at the surface [22]. Because shielding gas escapes from the nozzles with nonnegligible velocity, a heat transfer coefficient of 200 W $m^{-2}.K^{-1}$ [23] caused by forced convection is considered for the simulation.

The critical temperatures for the austenization phase transformation are calculated according to the model proposed by Stone et al. [24] using the element composition in Table 1 (Ac1=1148 K and Ac3=1355 K). The martensite start temperature is estimated using the model of Capdevila et al. [25], which is adjusted by the addition of Cr compared to the classic formula (Ms=841 K).

The same parameters are used to predict the temperature changes on the laser beam side. Fig. 4(a) shows the temperature evolution during the single laser treatment of the beam center on both the front and back surface for all the selected powers with Ar shielding gas. All front surface temperatures exceed Ac1. For all input powers, the temperature difference between the two surfaces is very pronounced, being more than 230 K. There is always a slight delay in the temperature change on the back surface during heating. Temperature changes during treatment with the double laser on both sides are shown in Fig. 4(b), with the fiber laser SPI on surface A and the diode laser DILAS on surface B. As the spot size of the DILAS laser is slightly larger than that of the SPI, the peak temperature is tens of K lower. For both conditions, the temperature evolution rates are very high, ranging from 1000 to 3000 K/s for heating and from 400 to 1000 K/s for cooling depending on the powers.

The temperatures and isothermals are illustrated in Fig. 5 with a LED of 20 kJ/m with (a) one laser and (b) double lasers. The gap between the highest and lowest temperatures through the thickness of the laser track center is around 260 K with a single laser compared to only around 10 K with the double lasers. Thus, the laser thermal treatment is distributed more uniformly throughout the thickness when two lasers are used from both sides.

3.2. Microstructure

Fig. 6 shows the AISI 430 base material without any laser treatment, which presents a complete equiaxed ferritic microstructure with evenly distributed chromium carbide precipitations with an average grain size

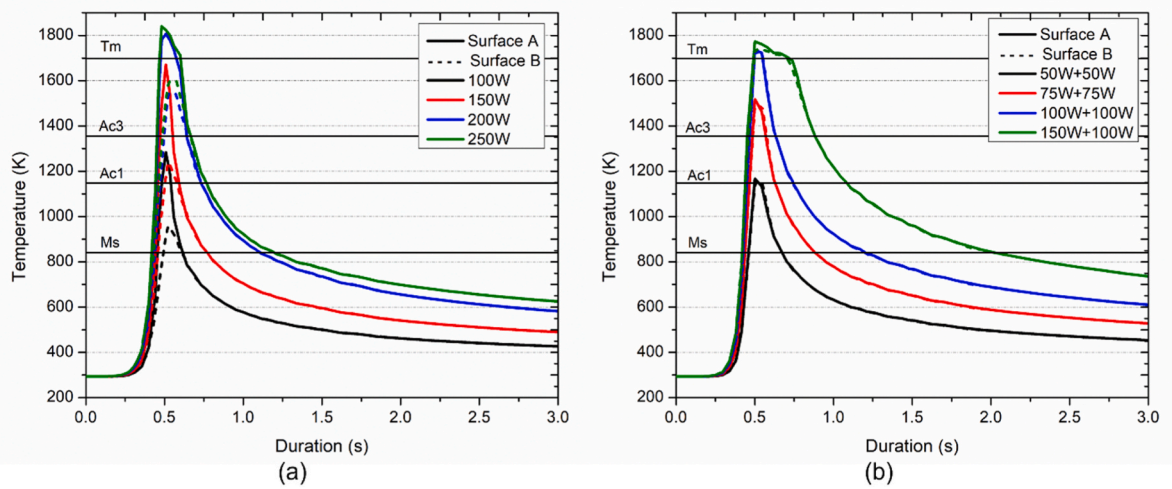

Fig. 4. Temperature evolution during laser treatment at different powers under Ar shielding gas (a) with a single laser and (b) with a laser on both sides.

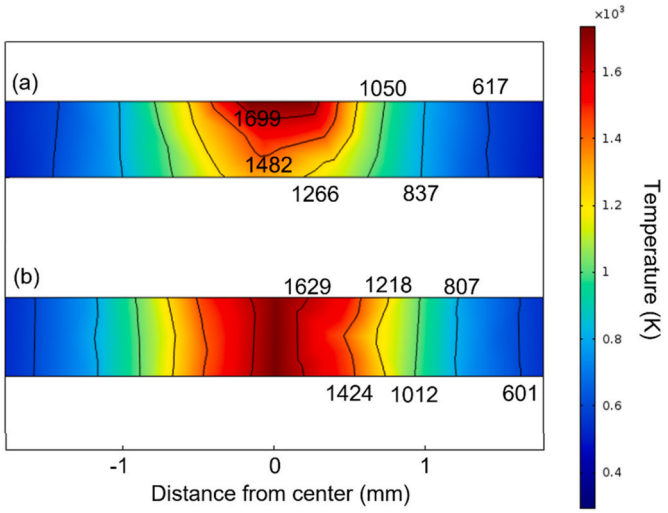

Fig. 5. Isothermals on the section of the laser track center under treatment in Ar using (a) 200 W with a single laser (b) 100 W + 100 W with two lasers.

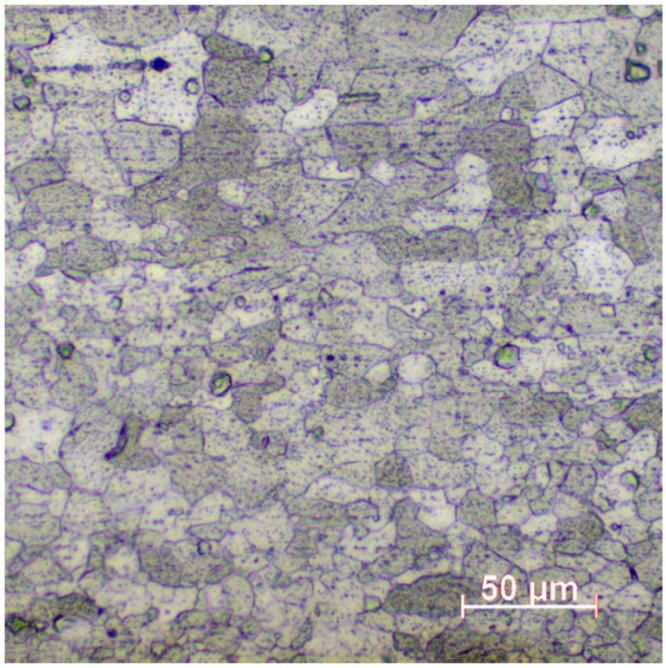

Fig. 6. Microstructure of the base material AISI 430.

of 11.3 μm. Fig. 7(a)-(h) is the macrograph of the single-track laser-treated area at different powers with Ar shielding gas. In (a) and (e), there is a slight growth of the grain size on the surface layer with 10 kJ/m. In (b) and (c), the grains in the middle of the treated zone are almost equiaxed and homogenous through the thickness by the symmetrical laser spots. In (f) and (g), grains near the front surface, where the laser is applied, are columnar in the normal direction of the arc-shaped treated zone. In (d) and (h), columnar grains are produced along the thickness in the center line and parallel to the adjacent surface. Columnar grains are formed along the solidification direction in a melt pool, because the high power (25 kJ/m) results in a total fusion in the treated zone. The columnar grains in (h) are more elongated than (d) due to the higher cooling rate. Grain size decreases progressively with the distance from the center, except for (a), where the laser powers on both sides are relatively low. No evident porosity is observed even for 25 kJ/m, where total fusion is achieved though the section.

With the same input LED, single and double laser treatments reveal rather different microstructures due to the thermal gradient and cooling rate. As described in section 3.1 above, with a symmetric double laser treatment (Fig. 7 (a)–(d)), both surfaces are irradiated so that the temperature is less gradient through the thickness, being equivalent to only tens of Ks. However, with the single laser treatment (Fig. 7 (e)–(h)), the temperature gradient between the irradiated and reverse sides is much higher, being a few hundreds of Ks. Thus, at the same LED, the double laser treatment yields a more uniform microstructure. As shown in Fig. 4, the cooling rate of the single laser (a) is nearly twice as high as that of the double laser (b), which favors the growth of the columnar grains upon cooling. With the same LED, more columnar grains appear in the treated zone.

The typical section microstructure can be described in three parts as shown in Fig. 9: the treated zone with dramatic grain coarsening that corresponds to the fusion zone in this case; the heat affected zone (HAZ) with a gradient of the grain size; and the base material (BM). There is no sharp boundary between each zone, and the transition is successional. Average grain sizes in the treated zone and HAZ in Fig. 7 (a)–(h) are depicted in Fig. 8(a), and those treated in air in Fig. 8(b). Average grain sizes in the treated zone and HAZ increase with the higher LED. For the double laser process, the grain coarsening is less dramatic in the treated zone, although the average grain size in HAZ is slightly larger. With the same LED, the average grain size is larger in air than in Ar due to the

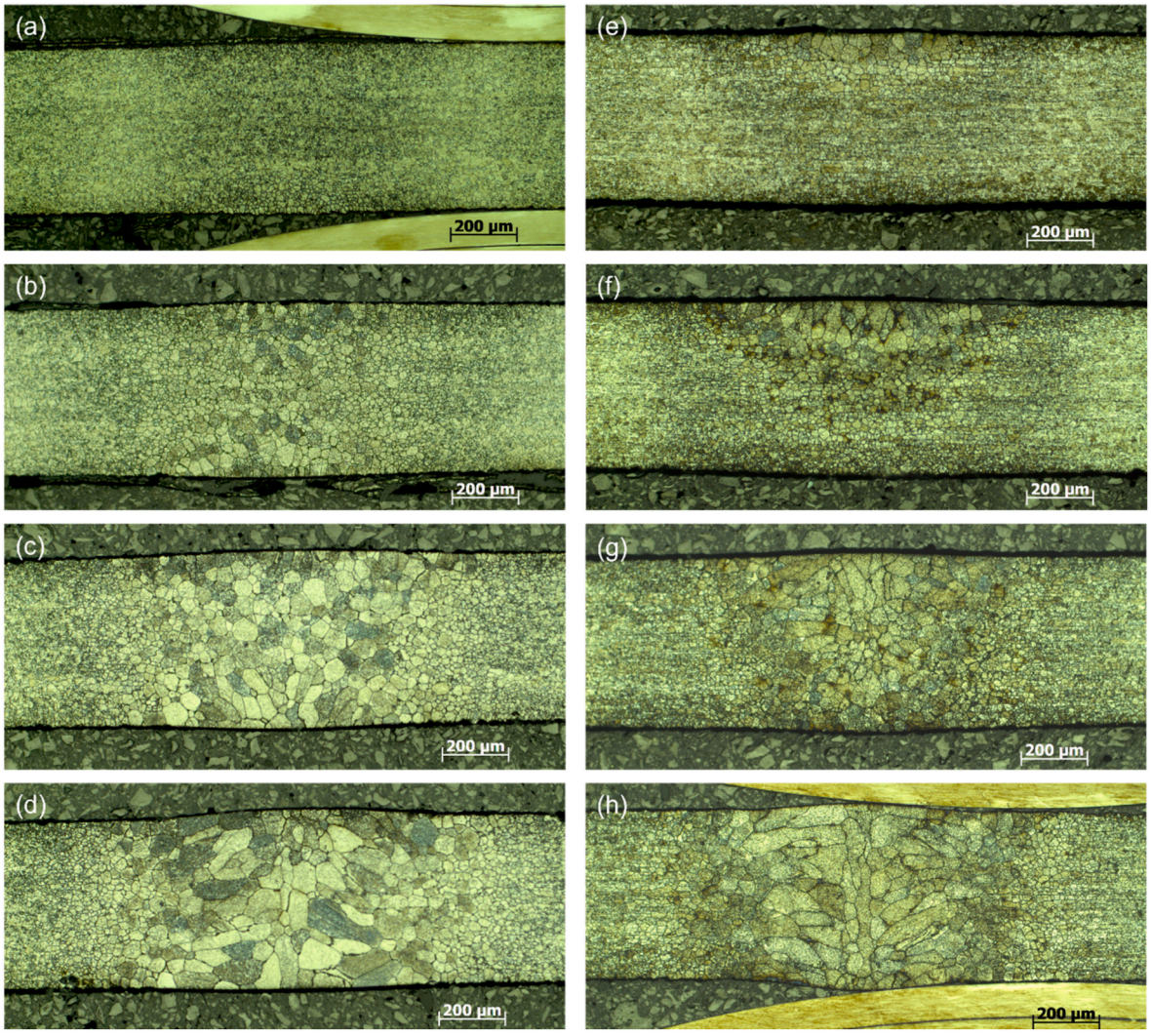

Fig. 7. Macrostructure of the single-track laser-treated area in Ar at (a) 50 W + 50 W, (b) 75 W + 75 W, (c) 100 W + 100 W, (d) 150 W + 100 W, (e) 100 W, (f) 150 W, (g) 200 W, and (h) 250 W.

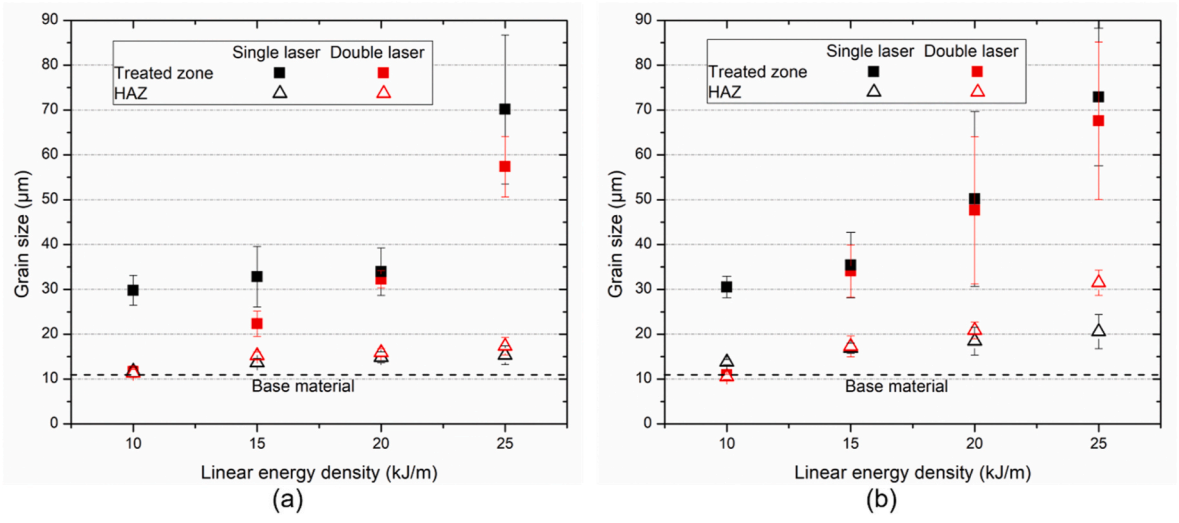

Fig. 8. Average grain size of the treated zone and HAZ in specimens treated at different LED in (a) Ar and (b) air.

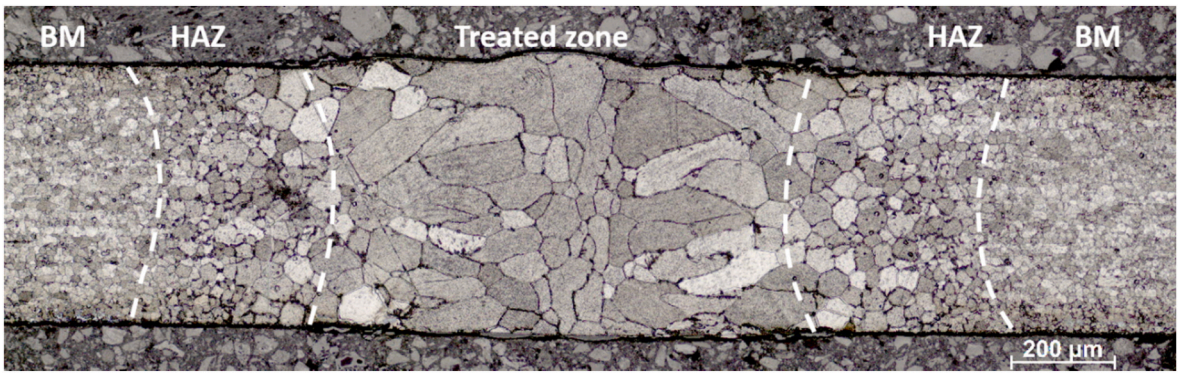

Fig. 9. Macrograph of the section of a single-track laser sample treated at 100 W from both sides in air.

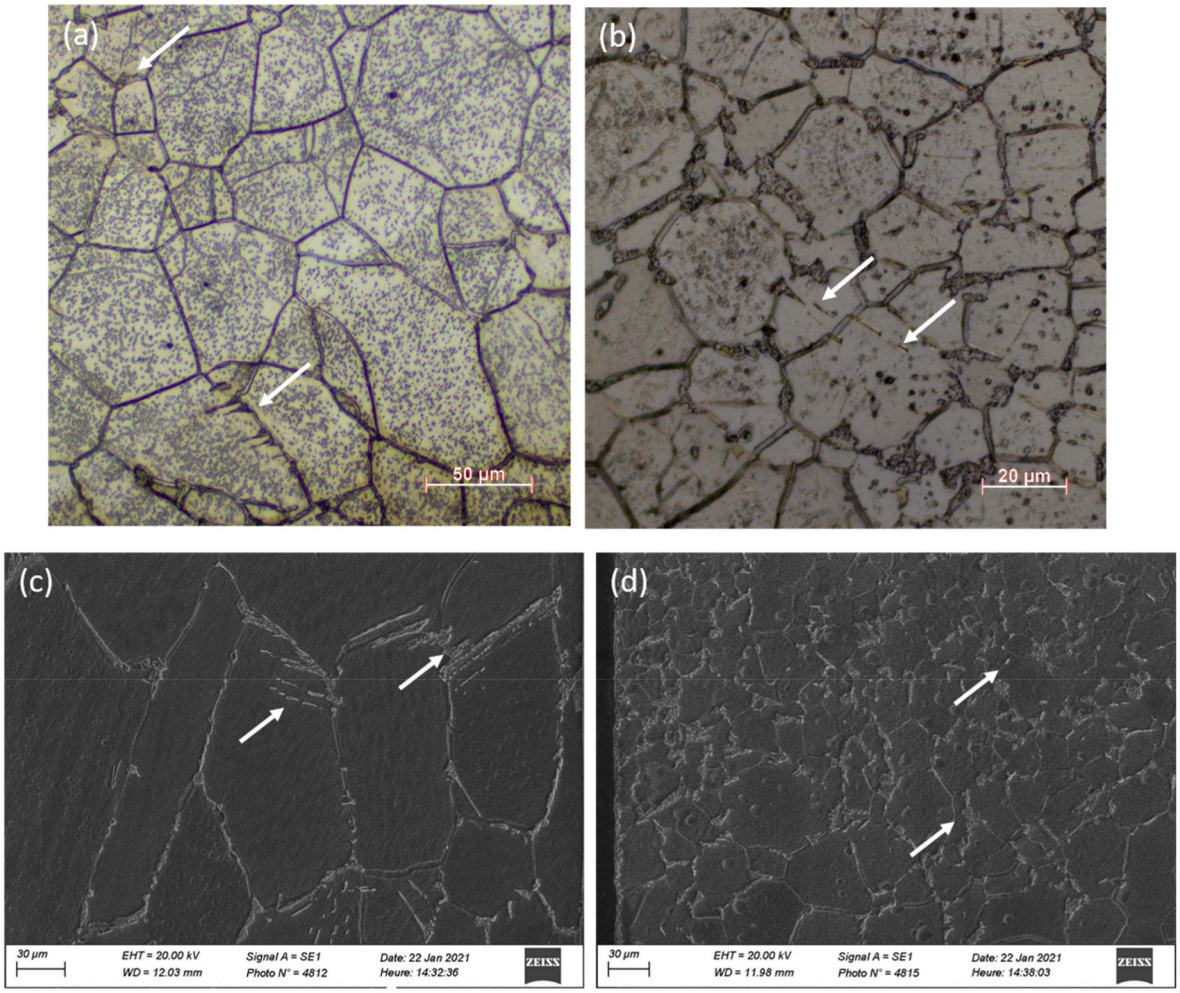

Fig. 10. Optical microscope showing the microstructure of a sample treated at 100 W from both sides in Ar at the (a) treated zone and (b) HAZ as well as SEM of a sample treated at 150 W + 100 W from both sides in air at the (c) treated zone and (d) HAZ.

higher laser absorption.

Studies on the optical microscope and SEM (Fig. 10) reveal that martensite formation occurs in the treated zone and HAZ in most circumstances (except for at the lowest power), principally with intergranular formations but sometimes with intragranular formations. With the higher input power, more martensite is formed. In the treated zone in Fig. 10(a), martensite is more needle-like, germinating along the new grain boundaries and growing toward the inside. A large quantity of carbides is found inside the grains, and the sub-grain boundaries are revealed. There is a carbide-free zone near the grain boundaries due to the local low carbon concentration. Carbon atoms in this zone are diffused in the austenite region at elevated temperatures, which transforms into martensite during rapid cooling [26].

In HAZ in Fig. 10(b) and (d), a few martensite needles can be found in the high-temperature heat affected zone (HT-HAZ), and some martensite islands are distributed at triple junctions in the low-temperature heat affected zone (LT-HAZ). This difference of phase presence can be explained by the temperature change. As the temperature at the treated

zone and HT-HAZ is much higher than Ac3, and the cooling is extremely rapid, austenite formation is insufficient to avoid grain coarsening [26]. In the LT-HAZ, the peak temperature is above Ac1, and the cooling rate is lower, meaning that a small amount of austenite has enough time to form along the ferrite grain boundaries, which are fixed by this germination. The entire HAZ shows a clear recrystallisation [27].

Microstructures of the samples treated in air and Ar shielding gas present similar properties. Nevertheless, due to the much higher absorption rate with oxidation, the HAZ in air is more expanded, which results in an overlapping HAZ between two laser tracks during the multi-track treatment.

3.3. Microhardness

The microhardness test shows that the base material presents a Vickers hardness of around 160 Hv. Fig. 11 reveals the hardness along the middle line of the section with a single-track (a) and multi-track (b) laser treatment at 100 W from the two sides in both air and Ar. Track centers are marked by dashed lines. With a single-track laser, a maximum hardness of around 310 Hv is produced in the treated zone, which is 90% higher than the base material. The hardened zone in Ar is narrower than in air, and the maximum value obtained is also lower. The hardened zone in Ar presents a wave-like profile with the peak values almost unchanged in the middle of each track, although the hardened zone in air presents a hardness that dropped to around 220 Hv, even for the laser track center.

For other conditions, except at 50 W from each side where the highest temperature in the adjacent layer of the sheets is below Ac1, microhardness also increases at the different levels. This softening with the multi-track laser treatment exists for samples with a high input power in both air and Ar, although in Ar the required power is higher (25 kJ/m).

3.4. Surface state

As the surface temperature during the treatment is relatively high (above Ac1 for the lowest power and above the melting point for the highest power), oxidation is not negligible. Fully treated samples are characterized by GD-OES to determine the thickness of the oxide layer on both surfaces after the laser treatment. The preliminary experiment indicates that the sputtering rate of GD-OES on this material with the selected argon pressure and RF power parameters is 0.068 μm/s, which is consistent with the sputtering rate reported in [28]. Fig. 12(a) allows us to observe the GD-OES depth profiles of major elements from the front surface to the adjacent layer of a sample at 200 W in air. The signal of oxygen is found to be stable around 19.4 μm after being amplified. Besides the signal of O, the signals of Cr and Mn are also stronger at the surface (around 3.4 μm) compared to the adjacent layer. However, the signal of Fe is weaker at the surface and increases with the erosion depth. As the main oxides formed are Cr_2O_3 and Fe_2O_3 [29], this evolution means that the formation of Cr_2O_3 is greater than that of Fe_2O_3 on the surface during high-temperature oxidation. This may be explained by the fact that the Gibbs free energy (ΔG°) to oxidate Cr is much more negative than for Fe, which makes it thermodynamically favorable to generate Cr_2O_3 [29]. This affinity for Cr oxidation may decrease the Cr concentration of the substrate metal. The same trend has been observed on all samples treated in air. The GD-OES depth profiles at the same power with Ar in Fig. 12(b) do not show the same evolution. The signals of all elements become stable in less than 2 μm, and there is no decrease for either Cr or Mn.

The thickness of the oxide layers on both surfaces of the samples in each condition is reported in Fig. 13. In Fig. 13(a), the thickness increases with the laser power before the temperatures of both sides reach the melting point (200 W and 250 W). The difference in thickness between the two surfaces is greater with the single laser at relatively low powers (9.0 μm more on the front surface for 150 W and 3.7 μm for 75 W from both sides), where temperatures differ more. The total thickness of both sides with double lasers is greater than that with a single laser at lower powers (35.4 μm for 75 W from both sides and 21.7 μm for 150 W), which can be explained by the lower temperatures on surface B. For the specimens heated above Tm, the thickness of the oxide layer almost stops increasing when the total thickness is around 38 μm. As the steel sheets are thin (0.5 mm), the oxidation is considerable (7.6%). In Fig. 11 (b), the oxide layer formed in Ar shielding gas is not greatly affected by the operation parameters, and the average thickness is only around 5.0 μm (1%), with a maximum value of 8.0 μm. This flaky and brittle oxide layer has an effect on mechanical behavior, which is discussed in the following section.

3.5. Tensile test

Fig. 14 shows the uniaxial tensile test results of the treated samples in air (a) and with Ar shielding gas (b). The base material presents ductile behavior with yield stress ($\sigma_{0.2\%}$) of around 350 MPa, ultimate tensile strength (UTS) of around 500 MPa, and uniform plastic deformation ε_u of 19.5%. With the temperature increase during laser treatment, the samples become more strengthened but less ductile.

As oxide increases the laser absorption rate [22], the peak

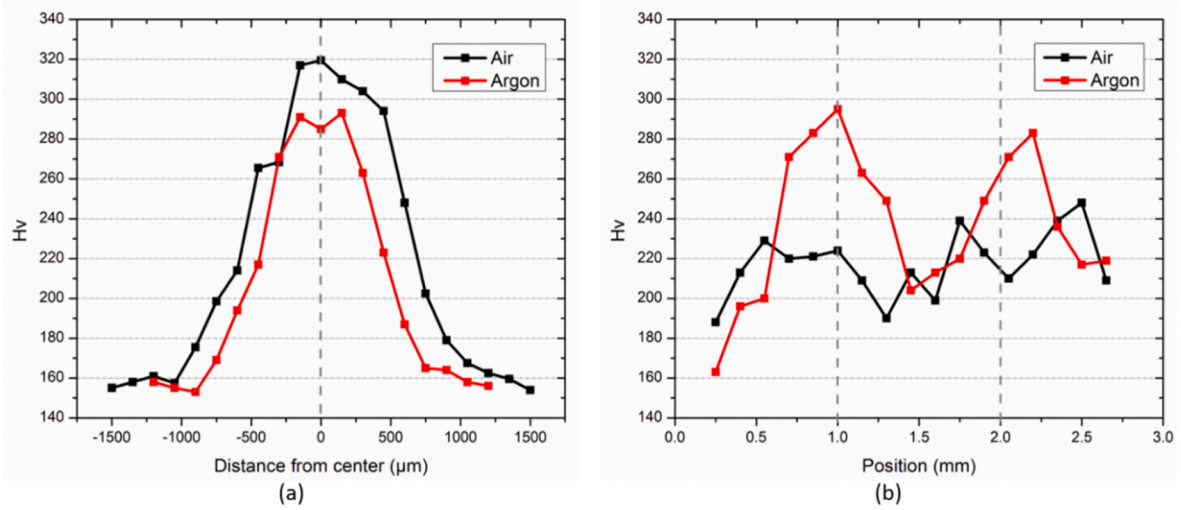

Fig. 11. Microhardness at the specimen core after (a) single-track and (b) multi-track laser treatment at 100 W from both sides.

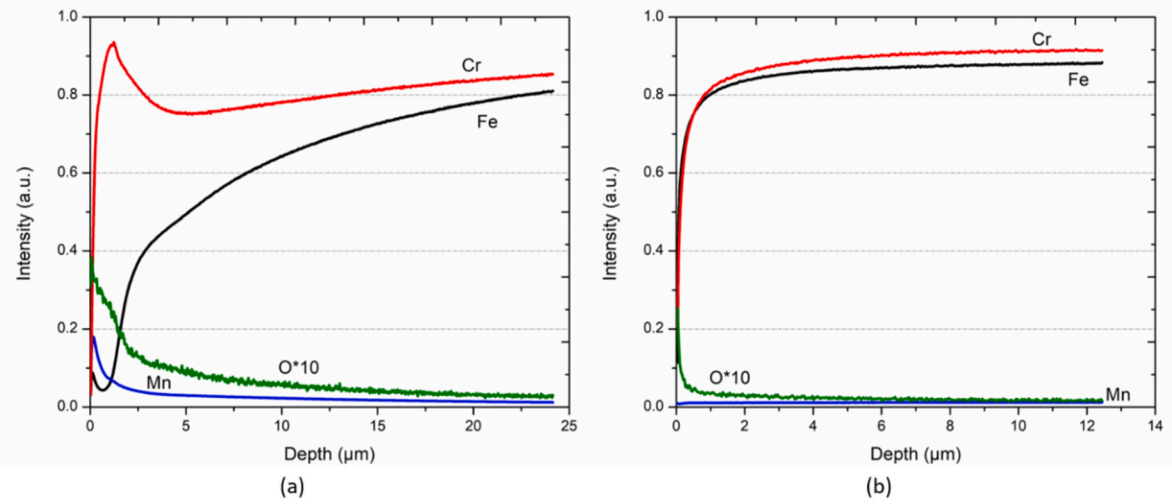

Fig. 12. GDOES signal of the front surface of a sample at 200 W (a) without and (b) with Ar shielding gas.

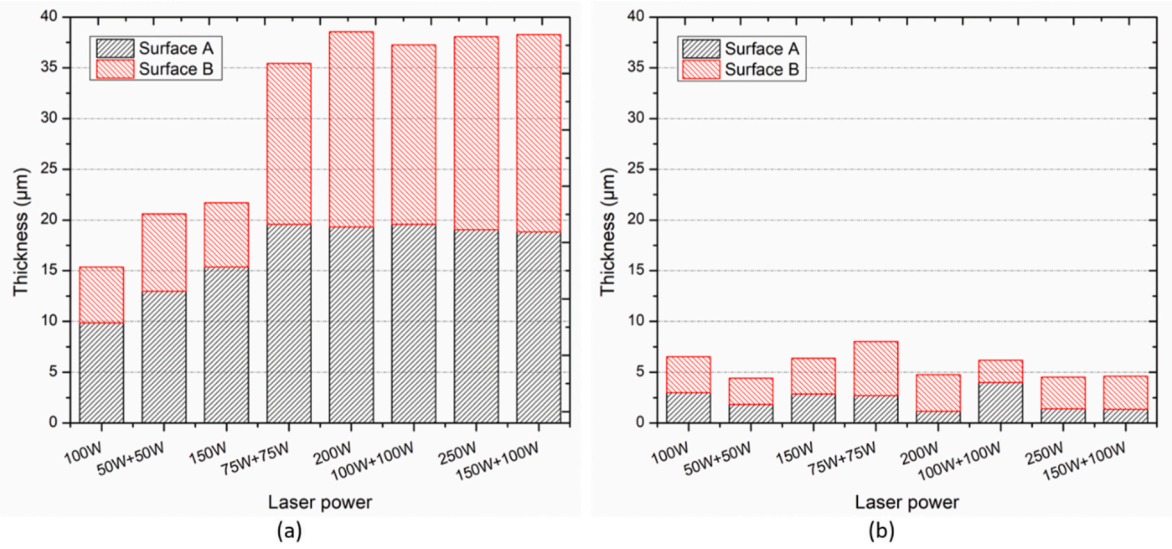

Fig. 13. Thickness of the oxide layers on both surfaces after laser treatment (a) without shielding gas and (b) with Ar shielding gas.

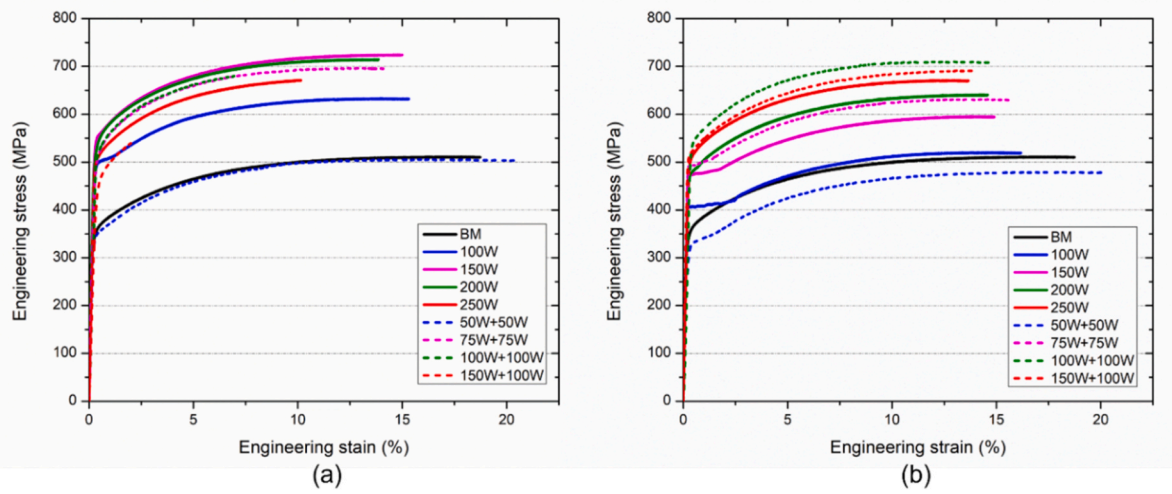

Fig. 14. Tensile test results of laser-treated samples (a) without shielding gas and (b) with Ar shielding gas.

temperatures are much higher with the same power in air than in Ar when the temperature is below Tm. At lower powers (100 W and 150 W), the strengthening effect in mechanical properties is more obvious. However, at higher powers in air as shown in Fig. 14(a), σ-ε curves begin to overlap at 150 W and become less ductile. In Fig. 14(b), the changes in properties at different powers are more dispersed. The strength continues to increase with higher powers until 250 W.

Fig. 15 shows (a) $\sigma_{0.2\%}$, (b) UTS, (c) ε_u, and (d) absorbed energy density for samples treated in each condition, where each point is the average value of four samples. In Fig. 15(a), all treated samples have a more elevated yield stress than the base material except for 50 W with two lasers. Obviously, $\sigma_{0.2\%}$ increases with a single laser at all chosen powers in air, with a maximum of 560 MPa (60% more than the base material) at 150 W and a minimum of 506 MPa at 100 W. However, for both treatments in air, $\sigma_{0.2\%}$ decreases after 150 W or 75 W on both sides. With shielding gas, $\sigma_{0.2\%}$ does not greatly change at lower powers (100 W or 50 W + 50 W) and begins to increase when raising the powers. With the single laser, $\sigma_{0.2\%}$ continues to increase, but with double lasers, it decreases at 150 W + 100 W.

Similar trends can be found for the UTS in Fig. 15(b). All treated samples have a higher UTS than the base material except for the lowest power in Ar. Without shielding gas, UTS increases when raising the laser power for both single and double laser beams. For a single laser beam, UTS reaches 729 MPa at 150 W and 200 W (45.8% more than the base material) and subsequently decreases. For double laser beams, the maximal value is 686 MPa at 75 W from both sides. With shielding gas, the gain in UTS with the double-face treated samples is more pronounced than with the single-face samples. UTS continuously improves with the single beam power and reaches 666 MPa at 250 W, although with 100 W from both sides, UTS is 702 MPa.

In Fig. 15(c), ε_u is worsened by laser treatment and decreases with the power growth in each condition by different levels. Laser treatment in air fragilizes the sample much more than in Ar shielding gas. ε_u is only 2.99% at 150 W + 100 W compared to 12–14% at the highest power in Ar.

Fracture energy density is shown in Fig. 15(d). Compared to the base material (91.3 MJ/m^3), laser treatment in Ar has a smaller effect on the fracture energy density (lowest 76.18 MJ/m^3 and highest 94.99 MJ/m^3), especially with two lasers. Treatment in air has a much more variable effect with 112.50 MJ/m^3 at 150 W and only 18.14 MJ/m^3 at 150 W + 100 W. Double lasers rapidly deteriorate the energy density at higher powers.

4. Discussion

4.1. Effect of microstructure on mechanical properties

Even though FSS are often considered to be non-hardenable [8], high power laser treatment can effectively increase the local microhardness of AISI 430. Despite dramatic grain coarsening in the treated zone, the maximum microhardness is caused by the substantial chromium carbide precipitates [30] and the martensite needles at the grain boundaries. Hardness decreases when moving away from the laser beam center due to less martensite formation and carbide precipitation. In Fig. 11(b), the

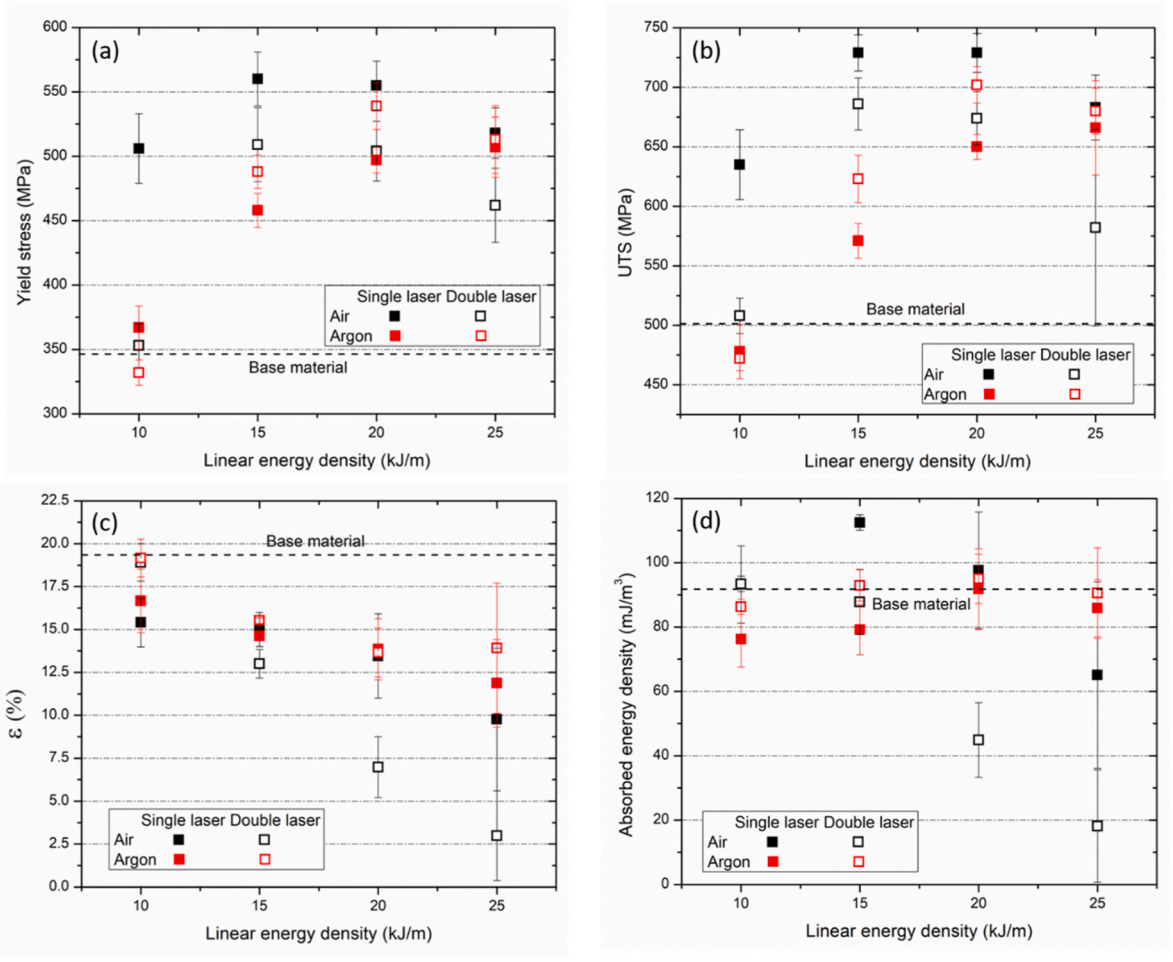

Fig. 15. Average (a) yield stress, (b) ultimate tensile strength, (c) uniform plastic deformation, and (d) absorbed energy density of the treated samples in each condition.

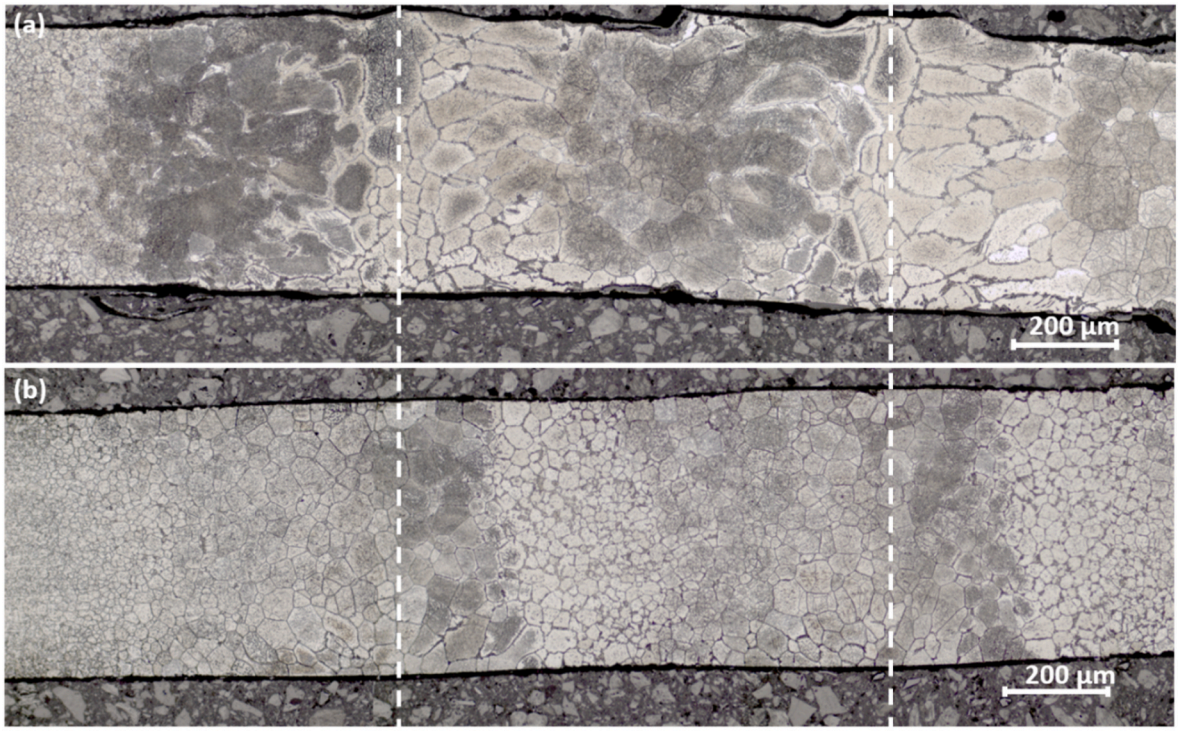

Fig. 16. Macrostructure of the multi-track section of specimens treated at 100 W on both sides (a) in air and (b) in Ar.

different profiles of microhardness in the samples treated in air and Ar can be explained by the effect of the adjacent tracks. Fig. 16 shows the macrostructures of the sections of specimens at 100W on both sides, with the positions of the beam centers marked by white dashed lines. The energy absorption in Ar is less, and as a result, the HAZ is much less expanded. A smaller zone along the former tracks is reheated by the adjacent ones above critical temperatures. On the one hand, the martensite formed during rapid cooling is softened by this reheating phase, which serves as tempering or annealing depending on the different distances [6,31]. On the other hand, the carbide precipitates are also partly dissolved into the matrix by the adjacent track [30].

The mechanical properties are summarized in Table 3 for the base material and specimens treated by double laser in Ar. With a higher LED, the average microhardness, $\sigma_{0.2\%}$, UTS, and absorbed energy density increase to peak values at 20 kJ/m and then decrease at 25 kJ/m. Results for other treatment conditions present similar trends with different optimal LED. ε_u continues to worsen with higher LED. When the surface temperature reaches Ac1, the superficial grains begin to coarsen but the underlying material is not heated enough to result in microstructure changes, meaning that the tensile behaviors are similar to the base material. With a higher input power, a larger underlying zone has reached Ac1, even Ac3. Coarsening equiaxed grains appear in the treated zone. $\sigma_{0.2\%}$ and UTS are well enhanced (maximum 60% and 45.8% increase, respectively) by martensite and carbides rich in Cr that are formed upon cooling, although ε_u is slightly reduced. When the temperature reaches Tm, dramatic anisotropic columnar grains are formed along the solidification direction. Such structures are susceptible to tearing and favor crack initiation and propagation along the grain boundaries and reduce the tensile properties [32,33]. At 25 kJ/m, a complete fusion is achieved through the depth, which widens the standard deviation. Solidification ripples on the surface also add instability to the mechanical properties. HAZ is broader at higher powers, martensite is tempered, and carbides are partly dissolved by adjacent laser tracks, which reduces $\sigma_{0.2\%}$ and UTS.

Table 3
Mechanical properties of the base material and samples treated by the double laser at different LED.

	Base material	10 kJ/m	15 kJ/m	20 kJ/m	25 kJ/m
Micro hardness (Hv)	160.0	158.0	211.5	241.8	233.6
$\sigma_{0.2\%}$ (MPa)	346.0	332.0	488.7	539.7	513.0
UTS (MPa)	502.9	472.0	623.5	702.5	680.6
ε_u (%)	19.39	19.17	15.52	13.65	13.91
Absorbed energy density (MJ/m^3)	91.30	86.31	92.92	94.99	90.53

4.2. *Effect of oxidation*

During the tensile test of samples treated in air, the flaky oxide layers on the weld-side surfaces crack and peel off before the final rupture, because they are less ductile than the substrate metal. This oxide layer may cause microcracks in the substrate-treated metal by several mechanisms. Due to the differential thermal expansion, internal stresses along the interfaces increase, and cracks can initiate in the brittle oxide layer and then penetrate into the substrate perpendicularly for several microns during cooling [34]. When the brittle film and the ductile substrate share a solid interface, cracks appear in the film when it is loaded mechanically, thus creating a premature facture in the substrate [35]. Nevertheless, the fracture and peeling of the oxide in the early stages reduce the specimen section, which causes local stress concentration. The strain is not uniformly distributed over the gage section, and the specimens crack earlier. Thus, without shielding gas, the brittle oxidation layer worsens the ductility at a faster rate with the same input power by introducing microcracks beneath the metal surface. These microcracks reduce the mechanical properties during the tensile test. The surface roughness is also worsened with the simultaneous increase in oxide thickness, especially at high powers above Tm, as shown in Fig. 14(a).

As mentioned above, the oxide layer increases the laser absorption coefficient by at least 50% and makes it cumbersome to properly manage the peak temperature during treatment. This also enlarges HAZ

on account of the higher absorption rate, so that the reheat effect is even more obvious. In this case, the oxide layer impedes the mechanical behavior of the samples and adds uncertainties to the procedure, thus making it important to control it.

The changes in the mechanical properties result from the combination of microstructure and surface state after the laser treatment. A proper equiaxed microstructure and a surface without thick oxidation led to a more enhanced resistance with lower ductility.

5. Conclusions

Microstructural and mechanical property changes of thin AISI 430 sheets were studied here under different treatment conditions relating to the linear energy density, inert shielding gas, and treatment sides. Several conclusions emerge from the study.

(1) Despite the poor carbon content and grain coarsening, the laser heat treatment was shown to enhance the mechanical behavior of 18% Cr FSS by the formation of martensite and chromium carbides during rapid cooling. Local microhardness can be increased by 90% at most using a single-track laser treatment. Fully treated samples by multi-track laser treatment are characterized for the first time, and the yield stress is increased by 60% and UTS by 45.8%.
(2) Thick oxide layers formed at high temperatures on the weld-side surfaces, especially above Tm, fragilize the laser-treated material and make the results less repeatable. Argon shielding gas is efficient to mitigate these disadvantages.
(3) Double-sided laser treatment enables a more homogeneous treatment through the thickness, hence allowing for an optimal trade-off between strengthening and loss of ductility.
(4) With the flexibility of the laser treatment trajectory and the small spot size, localized heat treatment can be achieved, thus enabling laser-based architecturing of metallic materials.

Data availability

The raw/processed data required to reproduce these findings cannot be shared at this time due to technical or time limitations.

CRediT authorship contribution statement

Zhige Wang: Investigation, Methodology, Writing – original draft, preparation. **Justin Dirrenberger:** Conceptualization, Supervision, Methodology, Writing – review & editing. **Pierre Lapouge:** Investigation, Methodology, Writing – review & editing. **Sébastien Dubent:** Investigation, Methodology, Writing – review & editing.

Declaration of competing interest

The authors declare that they have no known competing financial interests or personal relationships that could have appeared to influence the work reported in this paper.

Acknowledgements

This study was funded by Agence Nationale de la Recherche through the ANR JCJC SCOLASTIC project (grant no. 16-CE08-0009).

References

[1] K.A. Cashell, N.R. Baddoo, Ferritic stainless steels in structural applications, Thin-Walled Struct. 83 (2014) 169–181, https://doi.org/10.1016/j.tws.2014.03.014.
[2] Y. Zhang, J. Guo, Y. Li, Z. Luo, X. Zhang, A comparative study between the mechanical and microstructural properties of resistance spot welding joints among ferritic AISI 430 and austenitic AISI 304 stainless steel, J. Mater. Res. Technol. 9 (2020) 574–583, https://doi.org/10.1016/j.jmrt.2019.10.086.
[3] H. Fu, J. Min, H. Zhao, Y. Xu, P. Hu, J. Peng, H. Dong, Improved mechanical properties of aluminum modified ultra-pure 429 ferritic stainless steels after welding, Mater. Sci. Eng. 749 (2019) 210–217, https://doi.org/10.1016/j.msea.2019.01.106.
[4] L.D. Tadepalli, A.M. Gosala, L. Kondamuru, S.C. Bairi, R. Subbiah, S.K. Singh, A review on effects of nitriding of AISI409 ferritic stainless steel, Mater. Today Proc. 26 (2020) 1014–1020, https://doi.org/10.1016/j.matpr.2020.01.299.
[5] E. Capello, B. Previtali, Enhancing dual phase steel formability by diode laser heat treatment, J. Laser Appl. 21 (2009) 1–9, https://doi.org/10.2351/1.3071316.
[6] P. Lapouge, J. Dirrenberger, F. Coste, M. Schneider, Laser heat treatment of martensitic steel and dual-phase steel with high martensite content, Mater. Sci. Eng. 752 (2019) 128–135, https://doi.org/10.1016/j.msea.2019.03.016.
[7] E. Kennedy, G. Byrne, D.N. Collins, A review of the use of high power diode lasers in surface hardening, J. Mater. Process. Technol. 155–156 (2004) 1855–1860, https://doi.org/10.1016/j.jmatprotec.2004.04.276.
[8] K.H. Lo, F.T. Cheng, H.C. Man, Laser transformation hardening of AISI 440C martensitic stainless steel for higher cavitation erosion resistance, Surf. Coating. Technol. 173 (2003) 96–104, https://doi.org/10.1016/S0257-8972(03)00347-5.
[9] M.O.H. Amuda, S. Mridha, Grain refinement and hardness distribution in cryogenically cooled ferritic stainless steel welds, Mater. Des. 47 (2013) 365–371, https://doi.org/10.1016/j.matdes.2012.12.008.
[10] G.L. Liu, S.W. Yang, W.T. Han, L.J. Zhou, M.Q. Zhang, J.W. Ding, Y. Dong, F. R. Wan, C.J. Shang, R.D.K. Misra, Microstructural evolution of dissimilar welded joints between reduced-activation ferritic-martensitic steel and 316L stainless steel during the post weld heat treatment, Mater. Sci. Eng. 722 (2018) 182–196, https://doi.org/10.1016/j.msea.2018.03.035.
[11] M.M.A. Khan, L. Romoli, G. Dini, Laser beam welding of dissimilar ferritic/martensitic stainless steels in a butt joint configuration, Opt Laser. Technol. 49 (2013) 125–136, https://doi.org/10.1016/j.optlastec.2012.12.025.
[12] Z. Zhang, Z. Wang, W. Wang, Z. Yan, P. Dong, H. Du, M. Ding, Microstructure evolution in heat affected zone of T4003 ferritic stainless steel, Mater. Des. 68 (2015) 114–120, https://doi.org/10.1016/j.matdes.2014.12.018.
[13] M.M.A. Khan, L. Romoli, M. Fiaschi, G. Dini, F. Sarri, Laser beam welding of dissimilar stainless steels in a fillet joint configuration, J. Mater. Process. Technol. 212 (2012) 856–867, https://doi.org/10.1016/j.jmatprotec.2011.11.011.
[14] S. Vafaeian, A. Fattah-alhosseini, Y. Mazaheri, M.K. Keshavarz, On the study of tensile and strain hardening behavior of a thermomechanically treated ferritic stainless steel, Mater. Sci. Eng. 669 (2016) 480–489, https://doi.org/10.1016/j.msea.2016.04.050.
[15] B.K. Jha, P. Jha, C.D. Singh, Process technology for the continuous hot band Annealing of 17%Cr ferritic stainless steel, J. Mater. Eng. Perform. 11 (2002) 180–186, https://doi.org/10.1361/105994902770344240.
[16] J. Sundqvist, T. Manninen, H.-P. Heikkinen, S. Anttila, A.F.H. Kaplan, Laser surface hardening of 11% Cr ferritic stainless steel and its sensitisation behaviour, Surf. Coating. Technol. 344 (2018) 673–679, https://doi.org/10.1016/j.surfcoat.2018.04.002.
[17] E. Taban, E. Deleu, A. Dhooge, E. Kaluc, Laser welding of modified 12% Cr stainless steel: strength, fatigue, toughness, microstructure and corrosion properties, Mater. Des. 30 (2009) 1193–1200, https://doi.org/10.1016/j.matdes.2008.06.030.
[18] B. Mahmoudi, M.J. Torkamany, A.R.S.R. Aghdam, J. Sabbaghzade, Laser surface hardening of AISI 420 stainless steel treated by pulsed Nd:YAG laser, Mater. Des. 31 (1980-2015) 2553–2560, https://doi.org/10.1016/j.matdes.2009.11.034, 2010.
[19] H. Pantsar, V. Kujanpää, Diode laser beam absorption in laser transformation hardening of low alloy steel, J. Laser Appl. 16 (2004) 147–153, https://doi.org/10.2351/1.1710879.
[20] M.O.H. Amuda, S. Mridha, Comparative evaluation of grain refinement in AISI 430 FSS welds by elemental metal powder addition and cryogenic cooling, Mater. Des. 35 (2012) 609–618, https://doi.org/10.1016/j.matdes.2011.09.066.
[21] J.-M. Franssen, P.V. Real, Fire Design of Steel Structures: Eurocode 1: Actions on Structures Part 1-2 - General Actions - Actions on Structures Exposed to Fire Eurocode 3: Design of Steel Structures Part 1-2 -, Wiley-VCH Verlag GmbH & Co. KGaA, Weinheim, Germany, 2010, https://doi.org/10.1002/9783433601570.
[22] F. Dausinger, J. Shen, Energy coupling efficiency in laser surface treatment, ISIJ Int. 33 (1993) 925–933, https://doi.org/10.2355/isijinternational.33.925.
[23] M. Narazaki, M. Kogawara, Q. MING, Y. Watanabe, Measurement and database construction of heat transfer coefficients of gas quenching, Strojniski Vestnik 55 (2009) 167–173.
[24] American Welding Society, Alloy composition and critical temperatures in type 410 steel welds, Weld. J. 97 (2018) 286–296, https://doi.org/10.29391/2018.97.025.
[25] C. Capdevila, F.G. Caballero, C.G. de Andrés, Determination of ms temperature in steels: a bayesian neural network model, ISIJ Int. 42 (2002) 894–902, https://doi.org/10.2355/isijinternational.42.894.
[26] M. Alizadeh-Sh, S.P.H. Marashi, M. Pouranvari, Resistance spot welding of AISI 430 ferritic stainless steel: phase transformations and mechanical properties, Mater. Des. 56 (1980-2015) 258–263, https://doi.org/10.1016/j.matdes.2013.11.022, 2014.
[27] X. Zhang, Y. Zhang, Y. Wu, S. Ao, Z. Luo, Effects of melting-mixing ratio on the interfacial microstructure and tensile properties of austenitic–ferritic stainless steel joints, J. Mater. Res. Technol. 8 (2019) 2649–2661, https://doi.org/10.1016/j.jmrt.2018.12.025.
[28] ChJ. Rao, S. Ningshen, J. Philip, Atmospheric air oxidation of 9Cr-1Mo steel: depth profiling of oxide layers using glow discharge optical emission spectrometry, Spectrochim. Acta Part B At. Spectrosc. 172 (2020) 105973, https://doi.org/10.1016/j.sab.2020.105973.

[29] C.Y. Cui, X.G. Cui, X.D. Ren, M.J. Qi, J.D. Hu, Y.M. Wang, Surface oxidation phenomenon and mechanism of AISI 304 stainless steel induced by Nd:YAG pulsed laser, Appl. Surf. Sci. 305 (2014) 817–824, https://doi.org/10.1016/j.apsusc.2014.04.025.
[30] S. Ghorbani, R. Ghasemi, R. Ebrahimi-Kahrizsangi, A. Hojjati-Najafabadi, Effect of post weld heat treatment (PWHT) on the microstructure, mechanical properties, and corrosion resistance of dissimilar stainless steels, Mater. Sci. Eng. 688 (2017) 470–479, https://doi.org/10.1016/j.msea.2017.02.020.
[31] L.R.C. Malheiros, E.A.P. Rodriguez, A. Arlazarov, Mechanical behavior of tempered martensite: characterization and modeling, Mater. Sci. Eng. 706 (2017) 38–47, https://doi.org/10.1016/j.msea.2017.08.089.
[32] L. Wang, M. Gao, C. Zhang, X. Zeng, Effect of beam oscillating pattern on weld characterization of laser welding of AA6061-T6 aluminum alloy, Mater. Des. 108 (2016) 707–717, https://doi.org/10.1016/j.matdes.2016.07.053.
[33] A. Faye, Y. Balcaen, L. Lacroix, J. Alexis, Effects of welding parameters on the microstructure and mechanical properties of the AA6061 aluminium alloy joined by a Yb: YAG laser beam, J. Adv. Join. Process. 3 (2021) 100047, https://doi.org/10.1016/j.jajp.2021.100047.
[34] H.M. Espejo, D.F. Bahr, Substrate cracking in Ti-6Al-4V driven by pulsed laser irradiation and oxidation, Surf. Coating. Technol. 322 (2017) 46–50, https://doi.org/10.1016/j.surfcoat.2017.05.001.
[35] T. Guo, L. Qiao, X. Pang, A.A. Volinsky, Brittle film-induced cracking of ductile substrates, Acta Mater. 99 (2015) 273–280, https://doi.org/10.1016/j.actamat.2015.07.059.